Manuscript submitted to
AIMS' Journals
Volume **X**, Number **0X**, XX **200X**

Website: http://AIMsciences.org

pp. **X–XX**

VIDEO STABILIZATION OF ATMOSPHERIC TURBULENCE DISTORTION

Yifei Lou

Department of Mathematics
University of California Los Angeles
Los Angeles, CA, 90095, USA

Sung Ha Kang

School of Mathematics
Georgia Institute of Technology
Atlanta, GA, 30332 USA

Stefano Soatto

Computer Science Department
University of California Los Angeles
Los Angeles, CA, 90095, USA

Andrea L. Bertozzi

Department of Mathematics
University of California Los Angeles
Los Angeles, CA, 90095, USA

(Communicated by the associate editor name)

Abstract. We present a method to enhance the quality of a video sequence captured through a turbulent atmospheric medium. Enhancement is framed as the inference of the radiance of the distant scene, represented as a "latent image," that is assumed to be constant throughout the video. Temporal distortion is thus zero-mean and temporal averaging produces a blurred version of the scene's radiance, that is processed via a Sobolev gradient flow to yield the latent image in a way that is reminiscent of the "lucky region" method. Without enforcing prior knowledge, we can stabilize the video sequence while preserving fine details. We also present the well-posedness theory for the stabilizing PDE and a linear stability analysis of the numerical scheme.

1. **Introduction.** Images of distant scenes, common in ground-based surveillance and astronomy, are often corrupted by atmospheric turbulence. Figure 1 shows sample frames from two video sequences of a synthetic target against a backdrop of trees, taken from a distance of 1Km at a rate of 30 frames per second (FPS). The first row (a)-(c) is taken in the morning and the second row (d)-(f) in the afternoon, when the effects of atmospheric turbulence are more severe.

There are several different models of image formation under atmospheric turbulence. In [8, 10, 28], a model of the form

$$f_k = D_k(K_k(f_k^{ideal})) + n_k$$

2000 *Mathematics Subject Classification.* Primary: 58F15, 58F17; Secondary: 53C35.

Key words and phrases. Imaging through turbulence, Sobolev gradient sharpening, anisotropic diffusion, spectral methods.

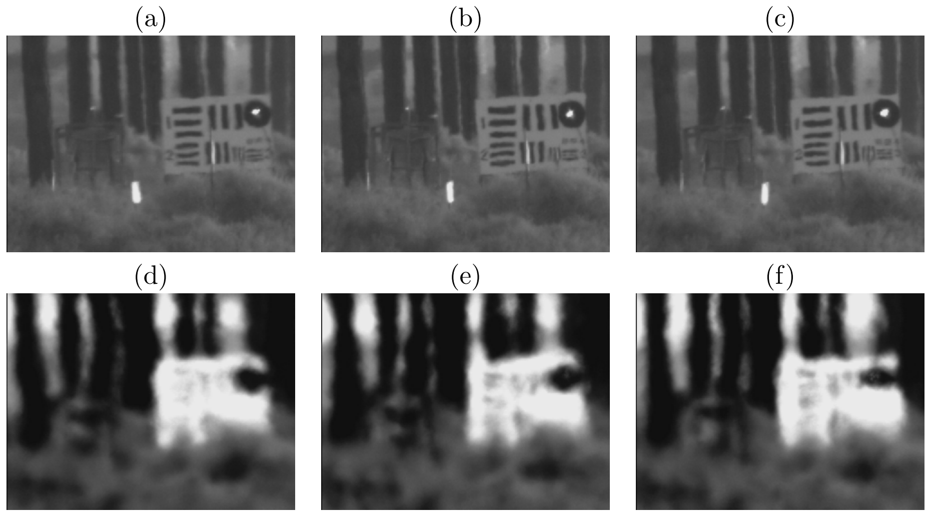

FIGURE 1. Examples of two video sequences distorted by atmospheric turbulence. The first row of images (a)-(c) is taken in the morning and the second row of images(d)-(f) is taken in the afternoon. Atmospheric turbulence causes both distortion of the domain of the images (warping) as well as diffusive degradation of the range of the images (blurring) that wash out fine details.

is used, where K represents the blurring kernel, D represents geometric distortion and n represents the additive noise, all of which can be different in each of the $k = 1, \dots N$ frames of the video sequence. Based on this model, the majority of approaches consider some diffeomorphic warping and image sharpening techniques: first a median filter is applied to find a good reference image, and geometric distortions are found via non-rigid registration, then the image is sharpened using blind or non-blind deconvolution, as in [8, 10]. In [23], to recover a high resolution latent image (f^{ideal}), a further super resolution method is applied. In [14], the authors explored two cases, FRD (finding diffeomorphism then deblurring) and DFG (each frame is deblurred, and then a diffeomorphism is considered). The DFG method usually yields more accurate reconstruction of the latent image. An extension to a variational model using Bregman iteration and operator splitting with optical flow is considered in [17]. In [29], the authors used B-spline for non-rigid registration and produce images from the registered frames, then blind deconvolution is applied; other relevant prior work includes [27, 28] and references therein.

Fried [9] considered the modulation transfer function for long and short exposure images, and related the statistics of wave distortion to optical resolution. This is in agreement with [13] on the long-term effect of turbulence in optical imaging, and field experiments are considered in [5]. An extension on the tile effect in short exposure is considered in [24]. A correlated imaging system is studied in [26], where analytical expressions for turbulence effects are derived. The authors of [11] used the Fried kernel and a framelet based deconvolution to find the latent image. Many deblurring techniques can be applied to find a sharp latent image such as in [11, 12, 19]. Other references and related works include [15, 16, 21, 22].

Another class of the reconstruction methods employs the ideas from image selection and data fusion to produce a high quality latent image. The "lucky frame" method [25] selects the best frame from a video stream using sharpness to measure the image quality. Since it is unlikely that there exists a frame that is sharp everywhere, Aubailly *et. al.* [2] proposed the Lucky-Region method which is a local version of the lucky frame method.

In this paper, we propose a simple and numerically stable method to unwarp the video and reconstruct a sharp latent image. Two of the main effects of atmospheric turbulence are temporal oscillation and blurry image frames. We propose to apply video frame sharpening and temporal diffusion at the same time. We apply a Sobolev gradient method [6] to sharpen individual frames and mitigate the temporal distortions by the Laplace operator. This eliminates explicit registration that can be computationally expensive. Furthermore, we use the reconstructed video to construct the latent image when the camera is stationary and the scene is static. We apply an approach related to the lucky-region method but with a different quality criterion to reconstruct a even sharper and more accurate image.

The paper is organized as follows. In Section 2, we review an image sharpening method via Sobolev gradient flow [6], and prove the existence and uniqueness of the solution. The new approach is discussed in Section 3. We consider the video reconstruction and stabilization, and finding the latent image. Numerical experiments are given in Section 4, which is followed by concluding remarks in Section 5.

2. Sobolev sharpening flow.

The heat flow for $u : \Omega \subset \mathbb{R}^2 \to \mathbb{R}$ is the gradient descent for the functional

$$E(u) = \frac{1}{2}\int_\Omega \|\nabla u\|^2 = \frac{1}{2}\|\nabla u\|_2^2 \ ,$$

with respect to the L^2 metric. An alternative gradient flow can be derived relative to the Sobolev metric. Let Ω be an open subset of $\mathbb{R}^2$ with smooth boundary $\partial\Omega$ and $\|\cdot\|_2$ be the L^2 norm integrated over Ω. An inner product on the Sobolev space $H^1(\Omega)$ can be defined as $\langle v, w\rangle \longrightarrow g_\lambda(v,w) = (1-\lambda)\langle v,w\rangle_{L^2} + \lambda\langle v,w\rangle_{H^1}$ for any $\lambda > 0$. The Sobolev metric g_λ on $H^1(\Omega)$ is given by

$$\nabla_{g_\lambda} E|_u = -\Delta(Id - \lambda\Delta)^{-1} u \ ,$$

where Id denotes the identity operator. Calder *et. al.* [6] introduce this idea for image processing and prove the well-posedness of the linear Sobolev gradient flow (SOB), *i.e.*,

$$u_t = \Delta(Id - \lambda\Delta)^{-1} u \ , \tag{1}$$

in both forward and backward directions. This can be easily understood via the Fourier transform,

$$\hat{u}_t = \frac{-4\pi^2|\xi|^2}{1 + 4\pi^2\lambda|\xi|^2}\hat{u} \ , \tag{2}$$

where the "hat" ˆ denotes the Fourier transform with frequency coordinate ξ. Note that the Fourier coefficients are uniformly bounded on any time interval, thus making the problem (1) well-posed for all Sobolev spaces.

As the backward direction can be used for image sharpening, Calder *et. al.* propose the following model:

$$E_s(u) = \frac{1}{4}\|\nabla u^0\|_2^2 \left(\frac{\|\nabla u\|_2^2}{\|\nabla u^0\|_2^2} - \alpha\right)^2 , \tag{3}$$

where u^0 is the initial condition and α is a scale: for $\alpha < 1$, we get blurring and for $\alpha > 1$ we get sharpening. The gradient descent partial differential equation (PDE) for the above functional with respect to the Sobolev metric is

$$u_t = \left(\frac{\|\nabla u\|_2^2}{\|\nabla u^0\|_2^2} - \alpha \right) \Delta (Id - \Delta)^{-1} u \ . \tag{4}$$

This is a nonlinear PDE. Its stopping time is implicitly encoded into the sharpness factor α, as the gradient descent stops when the ratio of $\|\nabla u\|_2^2$ to $\|\nabla u^0\|_2^2$ is α. We prove the existence and uniqueness of its solution in the next subsection, while the analysis of the linear PDE (1) is given in [6].

2.1. **Existence and uniqueness of the solution to (4).** We rewrite the nonlinear PDE in (4) as follows

$$\begin{cases} u_t = (\|\nabla u\|_2^2 - \alpha)\Delta(Id - \lambda\Delta)^{-1} u \ , \\ u(\cdot, 0) = u^0, \ \text{with } u^0 \in H^1(\Omega) \text{ and } \|\nabla u^0\|_2 = 1. \end{cases} \tag{5}$$

Theorem 2.1 (Local existence and uniqueness)**.** *Problem (5) has a unique solution in $C\big([0,T]; H^1(\Omega)\big)$ for some $T > 0$.*

Proof. Note that

$$\frac{du}{dt} = F(u) \ , \text{where } F(u) = (\|\nabla u\|_2^2 - \alpha)\Delta(Id - \Delta)^{-1} u \ ,$$

defines an ODE on the Banach space $H^1(\Omega)$. We want to show F is locally Lipschitz continuous on $H^1(\Omega)$ in order to use the Picard Theorem on a Banach space.

We first examine the L^2 norm,

$$\begin{aligned} \|F(u) - F(v)\|_2 \ \leqslant \ & \big| \|\nabla u\|_2^2 - \|\nabla v\|_2^2 \big| \cdot \|\Delta(Id - \lambda\Delta)^{-1} u\|_2 \\ & + \big| \|\nabla v\|_2^2 - \alpha \big| \cdot \|\Delta(Id - \lambda\Delta)^{-1}(u - v)\|_2 \ . \end{aligned} \tag{6}$$

Let $w = \Delta(Id - \lambda\Delta)^{-1} u$. It follows from Parseval's theorem that

$$\begin{aligned} & \|\Delta(Id - \lambda\Delta)^{-1} u\|_2^2 = \|w\|_2^2 = \|\hat{w}\|_2^2 = \sum_{\xi \in \mathbb{Z}^2} \frac{4\pi^2|\xi|^2}{1 + 4\pi^2\lambda|\xi|^2} |\hat{u}(\xi)|^2 \\ \leqslant \ & \frac{1}{\min(1,\lambda)} \sum_{\xi \in \mathbb{Z}^2} |\hat{u}(\xi)|^2 \ = \frac{\|u\|_2^2}{\lambda_0} \end{aligned}$$

where $\lambda_0 = \min(1, \lambda)$. Substituting the above inequality into (6), we have

$$\|F(u) - F(v)\|_2 \leqslant C_1 \|\nabla u - \nabla v\|_2 + C_2 \|u - v\|_2 \ , \tag{7}$$

with $C_1 = \frac{\|u\|_2}{\sqrt{\lambda_0}} \big| \|\nabla u\|_2 + \|\nabla v\|_2 \big|$ and $C_2 = \frac{1}{\sqrt{\lambda_0}} \big| \|\nabla v\|_2^2 - \alpha \big|$. Since the operators $\nabla, \Delta, (Id - \lambda\Delta)^{-1}$ commute, we can obtain a similar inequality for the H^1 seminorm,

$$\begin{aligned} & \|\nabla F(u) - \nabla F(v)\|_2 \\ \leqslant \ & \big| \|\nabla u\|_2^2 - \|\nabla v\|_2^2 \big| \frac{\|\nabla u\|_2}{\sqrt{\lambda_0}} + \Big| \|\nabla v\|_2^2 - \alpha \Big| \cdot \frac{\|\nabla u - \nabla v\|_2}{\sqrt{\lambda_0}} \\ \leqslant \ & \left(\frac{\|\nabla u\|_2}{\sqrt{\lambda_0}} \Big| \|\nabla u\|_2 + \|\nabla v\|_2 \Big| + \frac{\Big| \|\nabla v\|_2^2 - \alpha \Big|}{\sqrt{\lambda_0}} \right) \|\nabla u - \nabla v\|_2 \ . \end{aligned} \tag{8}$$

Combining inequalities (6) and (8), we have

$$\|F(u) - F(v)\|_{H^1} \leqslant C\|u - v\|_{H^1} \ , \tag{9}$$

where C depends on the H^1 norm of u and v. Therefore the local existence and uniqueness of the solution follows immediately from Picard theorem, since a Sobolev space is Banach. ☐

Theorem 2.2 (Global existence and uniqueness)**.** *Problem (5) has a global unique solution in* $C\big([0, +\infty); H^1(\Omega)\big)$*.*

Proof. Given the local existence of the solutions, we only need to show that the solution can be continued indefinitely. This requires an *a priori* bound for the H^1 norm of the solution u depending only on the initial data. We will discuss two cases as follows. Recall, $u_t = F(u)$, where $F(u) = (\|\nabla u\|_2^2 - \alpha)\Delta(Id - \Delta)^{-1}u$, and let $c(t) = \|\nabla u(t)\|_2^2 - \alpha$.

1. $\|\nabla u\|_2^2 \leqslant \alpha$.

   It follows from Poincare inequality that there exists a constant $C(\Omega)$ depending on Ω, such that

   $$\|u - \bar{u}\|_2 \leqslant C(\Omega)\|\nabla u\|_2 \ (\leqslant C(\Omega)\sqrt{\alpha}),$$

   where $\bar{u} = \frac{1}{|\Omega|}\int_\Omega u(y)\mathrm{d}y$. We find that $\bar{u}$ remains constant with respect to time, since

   $$\frac{d}{dt}\bar{u} = \frac{1}{|\Omega|}\int_\Omega u_t dy = \frac{c(t)}{|\Omega|}\int_\Omega \Delta(Id - \lambda\Delta)^{-1}u(y)dy = 0 \ .$$

   Then, using the triangular inequality with the initial condition u^0, we have the following bound,

   $$\|u\|_2^2 + \lambda\|\nabla u\|_2^2 \leqslant \big(\|\bar{u}^0\|_2 + C(\Omega)\sqrt{\alpha}\big)^2 + \lambda\alpha \ . \tag{10}$$

2. $\|\nabla u\|_2^2 > \alpha$.

   The time evolution of the L^2 norm of u has the expression

   $$\frac{1}{2}\frac{d}{dt}\|u\|_2^2 = \int_\Omega u u_t = c(t)\int_\Omega u\Delta(Id - \lambda\Delta)^{-1}u \ . \tag{11}$$

   Integrating by parts, we can obtain the time evolution of the H^1 semi-norm of u

   $$\begin{aligned}\frac{1}{2}\frac{d}{dt}\|\nabla u\|_2^2 &= -c(t)\int_\Omega \Delta u\Delta(Id - \lambda\Delta)^{-1}u \ , \\ &= -c(t)\int_\Omega u\Delta^2(Id - \lambda\Delta)^{-1}u \ ,\end{aligned} \tag{12}$$

   with the boundary condition, such as $u_t = 0$ on $\partial\Omega$ or Neumann boundary condition for u. We combine (11) and (12) in the following way,

   $$\begin{aligned}\frac{1}{2}\frac{d}{dt}(\|u\|_2^2 + \lambda\|\nabla u\|_2^2) &= c(t)\int_\Omega u(Id - \lambda\Delta)\Delta(Id - \lambda\Delta)^{-1}u \\ &= -c(t)\int u\Delta u = -c(t)\|\nabla u\|_2^2 \leqslant 0 \ .\end{aligned} \tag{13}$$

   This implies that $\|u\|_2^2 + \lambda\|\nabla u\|_2^2$ decreases as long as $\|\nabla u\|_2^2 > \alpha$.

Combining two cases, we have a bound for $\|u\|_2^2 + \lambda\|\nabla u\|_2^2$ to be $(\|\bar{u}^0\|_2 + C(\Omega)\sqrt{\alpha})^2 + \lambda\alpha$. This means that the constant C in (9) does not depend on the H^1 norm of u and v, which proves the global existence and uniqueness of the solution to (5). ☐

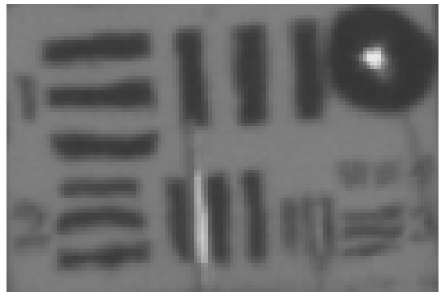

Figure 2. Close-up of the synthetic target (test board) in one video frames in Figure 1. Notice the boundaries of the rectangles display oscillations in space. They also exhibit oscillatory behavior in time, as one can see in the videos posted at https://sites.google.com/site/louyifei/research/turbulence.

3. **The proposed method.** We believe that the main challenge in dealing with atmospheric turbulence is the temporal undersampling that causes seemingly random temporal oscillations and blurring in each video frame. As shown in Figure 2, atmospheric turbulence makes the boundaries of rectangles oscillatory in the spatial domain as well as in time. Our main objective is to stabilize these oscillations in both space and time.

We compare the result of SOB (4) in Figure 3 with classical Perona-Malik (PM) anisotropic diffusion [20] and the shock filter [1]. Notice for PM, the edges are kept and smoothed along the direction of the boundaries of the rectangles without adding additional sharpening to the image result. The shock filter, on the other hand, is comprised of backward diffusion and a directional smoothing operator, thus yielding a sharp image reconstruction. Compared to Perona-Malik and the shock filter, the result of SOB, Figure 3 (d), looks more naturally sharp (although oscillations on the boundary still exist). This experiment motivates us to choose SOB as a sharpening method together with video stabilization. We will explain this in detail in Section 3.2.

We will also discuss the problem of recovering the latent image in Section 3.4. The results in Figure 3 (d), while sharp, show considerable residual oscillations. As in many approaches cited before, the median filter or temporal average is used as a baseline - for correcting object locations and stabilizing oscillations. Figure 4 shows these reconstruction techniques applied to the temporal average image. The result such as image (d) is a good latent image. Here the temporal average among the video sequence is computed, then Sobolev deblurring is applied to the temporal average. Compared to Figure 3, the boundaries are noticeably more straight by using the temporal average image.

3.1. **Assumptions on the turbulent imaging model.** Let the image domain be $\Omega \subset \mathbb{R}^2$, and the video sequence be $u(x, y, k)$ where k is the time index, and $(x, y) \in \Omega$: $u(x, y, k) : \Omega \times T \to \mathbb{R}^+$.

Atmospheric turbulent phenomena affect imaging data by distorting projection rays, thus inducing on the domain of the image a deformation (relative to the ideal medium). Such a deformation could be described by its infinitesimal generator, a vector field $v : \mathbb{R}^2 \to \mathbb{R}^2$, which in principle has non-trivial topology (sources,

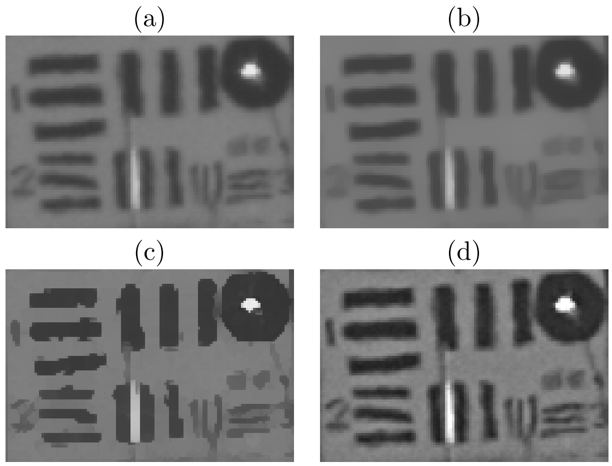

FIGURE 3. (a) one particular frame of the original video sequence, where (b) Perona and Malik [20] anisotropic diffusion is applied, (c) Shock filter [1], and (d) Sobolev gradient method [6]. Compared to (b) and (c), image (d) is more naturally sharp (although oscillations on the boundary still exist.)

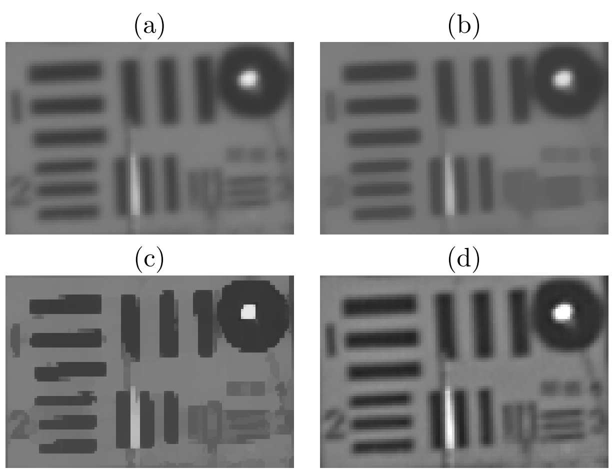

FIGURE 4. (a) The temporal average of 30 frames. (b) Perona and Malik [20] on (a). (c) Shock filter [1] applied to (a). (d) Sobolev gradient method [6] applied to image (a). In (b), PM shows sharp edges yet details are not well preserved. Image (c) is close to a piece-wise constant function yet shows stair-casing effects. Image (d) is more naturally sharp, while better preserving fine details.

sinks). However, because of temporal undersampling (image capture frequency is typically lower than the intrinsic temporal scale of atmospheric turbulent phenomena), there is a temporal averaging effect of fine-scale deformations that result in spatial blurring. We assume that the spatially blurred vector field has trivial topology, and it generates a diffeomorphism $w : \Omega \times T \subset \mathbb{R}^2 \times \mathbb{R}^+ \to \mathbb{R}^2$ which has zero mean displacement, i.e. for each $(x, y) \in \Omega$ we have that $\int_0^T w(x, y, k)\,\mathrm{d}k = 0$ for T sufficiently large.

Under these assumptions, we model turbulent imaging as blurring through a non-isotropic, non translation-invariant linear operator H that is the composition of an isotropic blur and a diffeomorphism: here $\bar{x}_i = (x_i, y_i, k)$,

$$H(\bar{x}_1, \bar{x}_2) \doteq \frac{h_\sigma(\bar{x}_1 - w^{-1}(\bar{x}_2))}{|J_w|}\ ,$$

where $|J_w|$ is the determinant of the Jacobian of special variables of w for a fixed time k, and $h_\sigma(\cdot)$ is an isotropic, static kernel, for instance a bi-variate Gaussian density

$$h_\sigma(\bar{x}_1 - \bar{x}_2) \doteq \frac{1}{\sqrt{2\pi}\sigma} \exp\left(-\frac{\|\bar{x}_1 - \bar{x}_2\|^2}{\sigma^2}\right).$$

Both $\sigma > 0$ and w are unknown; σ can vary depending on distance, time of the day, atmospheric conditions, otherwise constant both spatially and temporally on a small time-scale. The diffeomorphism w, on the other hand, can vary significantly both in space and in time. (It should be noted that the point-spread function neglects dependency on wavelength, although this could be included if multi-spectral sensing is available.)

We now describe the image formation model. We assume that the scene is Lambertian, which can be done without loss of generality since the scene is assumed to be seen from a stationary vantage point and constant illumination during the time-scale of observation. We call $\rho : S \subset \mathbb{R}^3 \to \mathbb{R}^+$ be the albedo of the scene, that is a function supported on a (piecewise smooth, multiply-connected) surface S, and is assumed to have a small total variation. Since we do not consider changes of vantage point (parallax), without loss of generality, we can assume S to be the graph of a function (depth map) parametrized with $(x, y) \in \Omega$. This can be expressed as $\rho : \mathbb{R}^2 \to \mathbb{R}^+$. Then, we can write the image-formation model as a convolution product between an isotropic static kernel and a warped version of the albedo:

$$u(x, y, k) = h_\sigma * \rho \circ w(x, y, k).$$

This can be verified with $\bar{x} = (x, y, k)$ that

$$\begin{aligned} h_\sigma * \rho \circ w(x, y, k) &= \int_{\mathbb{R}^2} h_\sigma(\bar{x} - \bar{y})\delta(z - w(\bar{y}))\rho(z)\mathrm{d}\bar{y}\mathrm{d}z \\ &= \int h_\sigma(\bar{x} - w^{-1}(z))\rho(z)\frac{1}{|J_w|}\mathrm{d}z \\ &= \int H(\bar{x}, z)\rho(z)\mathrm{d}z = u(\bar{x}). \end{aligned}$$

Therefore, atmospheric deblurring reduces to two independent problems, one of blind deconvolution and diffeomorphic blurring of a temporally under-sampled process w. We assume that each temporal instance of the vector field $\{w(\bar{x})\}_{(x,y)\in\Omega, k\in T}$ is an independent and identically distributed sample from a stochastic process. Therefore, we assume that there is no "predictive benefit" in knowing the history of the process w. A dynamic texture model to estimate the diffeomorphism w is discussed in [18].

3.2. **Video reconstruction/stabilization model.** The main idea of reconstructing atmospheric turbulence is to stabilize temporal oscillation while sharpening individual video frames. We propose the following PDE model for Video Stabilization (**SOB+LAP**):

$$u_t(x,y,k) = S[u(x,y,k)] + \mu\ \partial_{kk}u \tag{14}$$

where $S[\cdot]$ denotes a deblurring method on the spatial domain, and $\partial_{kk}u = u(x,y,k+1) - 2u(x,y,k) + u(x,y,k-1)$ is the Laplace operator in the time dimension k. From the comparisons in Figures 3 and 4, we apply the Sobolev approach (4) as the deblurring method.

Typically, isotropic diffusion is not well suited to preserve fine details. However, it performs well for time regularization in the case of video stabilization. This is due to the assumption that the camera is stationary and the scene is static. If anisotropic diffusion is applied in the time domain, it may lead to jumpy behaviors in time. Figure 5 illustrates this effect. From image (a), the red line profile is plotted in time in (b)-(d). Image (b) is the raw video sequence, while image (c) shows when three-dimensional Perona-Malik is applied to the (x,y,k)-direction, and image (d) shows when Perona-Malik is applied only on spacial direction of (x,y), and simple time Laplacian is applied to time direction. From this comparison, we can see that the space and time diffusion should be independent from each other, and using anisotropic diffusion for the time direction is not ideal.

We choose SOB (4) as a spatial sharpening method since it achieves the best performance in Figure 3 and 4. Furthermore, we apply the time Laplacian for temporal regularization, which also helps to remove the noise amplified by the sharpening method. The PDE evolution for SOB+LAP model goes as follows:

$$u_t = \left(\frac{\|\nabla u\|_2^2}{\|\nabla u^0\|_2^2} - \alpha \right) \Delta (Id - \lambda\Delta)^{-1} u + \mu\ \partial_{kk} u\ , \tag{15}$$

with u^0 the original video sequence, which is also the initial value for this PDE, and $\alpha > 1$ for deblurring from (3). Note that the Laplace operator Δ only acts on the spatial domain Ω. As for the parameter μ, it balances each individual frame deblurring with the temporal diffusion.

3.3. **Numerical scheme and stability analysis.** Calder *et. al.* [6] derive an explicit expression to compute the operator $(Id - \lambda\Delta)^{-1}$ on $\Omega = \mathbb{R}^2$, *i.e.*,

$$(Id - \lambda\Delta)^{-1} f(x) = S_\lambda * f(x), \quad \text{with} \quad S_\lambda(x) = \frac{1}{4\lambda\pi} \int_0^{+\infty} \frac{e^{-t - \frac{|x|^2}{4t\lambda}}}{t}\, \mathrm{d}t\ , \tag{16}$$

where $*$ denotes the convolution operator.

We assume periodic boundary conditions and formulate a spectral solver for eq. (15). Let $u_k(x,y) = u(x,y,k)$ and $\hat{u}_k^n(m_1,m_2)$ be the discrete Fourier transform of $u_k^n(x,y)$. We have

$$\frac{\hat{u}_k^{n+1} - \hat{u}_k^n}{dt} = C_k^n \frac{-4D(m_1,m_2)}{1 + 4\lambda D(m_1,m_2)} \hat{u}_k^n + \mu(\hat{u}_{k+1}^n + \hat{u}_{k-1}^n - 2\hat{u}_k^{n+1})\ , \tag{17}$$

$$\text{where} \qquad C_k^n = \frac{\sum_{m_1,m_2} D(m_1,m_2)|\hat{u}_k^n(m_1,m_2)|^2}{\sum_{m_1,m_2} D(m_1,m_2)|\hat{u}_k^0(m_1,m_2)|^2} - \alpha\ . \tag{18}$$

where $D(m_1,m_2) = \sin(\frac{m_1\pi}{M_1})^2 + \sin(\frac{m_2\pi}{M_2})^2$ for discrete coordinates $m_1 = 1, \cdots, M_1$ and $m_2 = 1, \cdots, M_2$.

(a) (b) (c) (d)

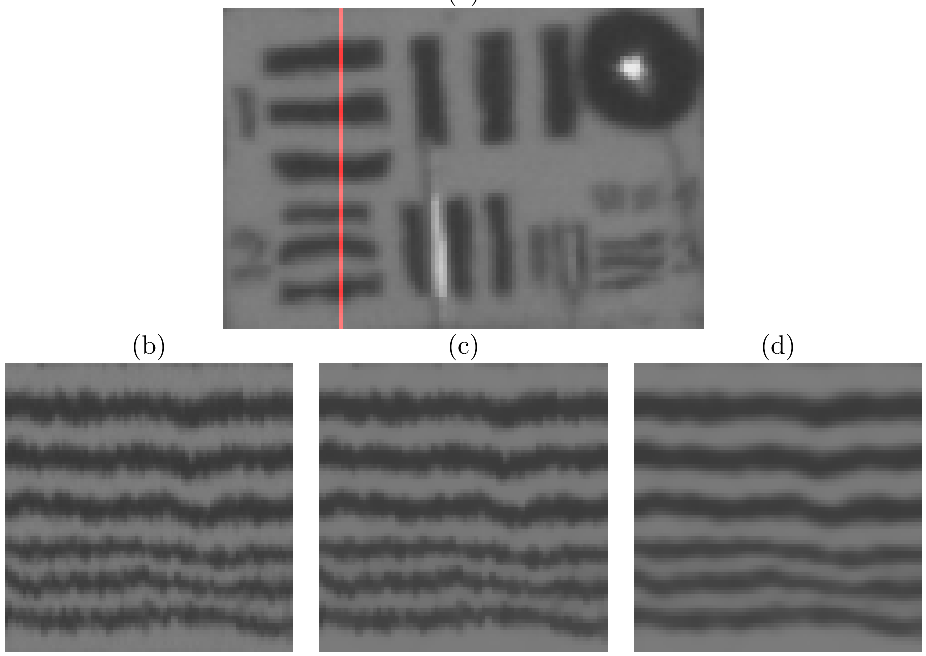

FIGURE 5. The comparison of temporal diffusion: (a) A given video frame at initial time $k = 1$. The red line is $u(x_1, y, 1)$ for a fixed x_1 and $\alpha \leq y \leq \beta$. (b) The plot of y vs k for the raw video frame: the plot of $u(x_1, y, k)$ with the fixed (vertical) location $\alpha \leq y \leq \beta$ and the varying time $1 \leq k \leq N$ (horizontal). (c) The plot of y vs k, after three-dimensional Perona-Malik is applied to (x, y, k). (d) The plot of y vs k, with Perona-Malik on (x, y) and the time Laplacian on k. Notice image (d) is more regularized than image (c). The time Laplacian regularizes the temporal direction better than anisotropic diffusion methods.

This approach yields a four-fold speed-up compared with the spatial domain calculation in (16). This is because our formulation is fully on the spectral domain, which only involves one pair of FFT and inverse FFT, while the evolution (16) has to perform convolution during each iteration.

For stability analysis, we linearize C_k^n in (17) with respect to $\hat{u}_k^n(m_1, m_2)$. Let $\tilde{u}(m_1, m_2)$ be the steady state of $\|\nabla \tilde{u}\|_2 = \alpha$. To simplify notations, we rescale the initial value u_k^0 such that $\|\nabla u_k^0\|_2 = 1$ and let $p(m_1, m_2) = \frac{4D(m_1,m_2)}{1+4\lambda D(m_1,m_2)}$. Substituting $\hat{u}_k^n = \tilde{u} + \epsilon v_k^n$ into eq. (17), we have

$$\begin{aligned} \frac{v_k^{n+1}(m_1, m_2) - v_k^n(m_1, m_2)}{dt} &= -2\left(\sum_{l_1,l_2} D(l_1, l_2)\tilde{u}(l_1, l_2)v_k^n(l_1, l_2)\right) p(m_1, m_2)\tilde{u}(m_1, m_2) + \\ &\quad +\mu(v_{k+1}^n(m_1, m_2) + v_{k-1}^n(m_1, m_2) - 2v_k^{n+1}(m_1, m_2)) + o(\epsilon). \end{aligned} \tag{19}$$

Multiplying $D(m_1, m_2)\tilde{u}(m_1, m_2)$ on both sides and summing over m_1, m_2, we get

$$\frac{z_k^{n+1} - z_k^n}{dt} = -2Az_k^n + \mu(z_{k+1}^n + z_{k-1}^n - 2z_k^{n+1}) \ , \tag{20}$$

where

$$z_k^n = \sum_{m_1, m_2} D(m_1, m_2)\tilde{u}(m_1, m_2)v_k^n(m_1, m_2)$$

$$A = \sum_{m_1, m_2} p(m_1, m_2)D(m_1, m_2)\tilde{u}^2(m_1, m_2) \geqslant 0.$$

Von Neumann stability analysis is conducted by replacing z_n^k with $g^n \exp^{ik\theta}$, *i.e.*,

$$\frac{g-1}{dt} = -2A + 2\mu(\cos\theta - g) \ .$$

The stability condition for (20) is that $|g| < 1$, which implies that $dt \leqslant 1/A$. This is a weak conditional stability in the sense that it is only for dt, not depending on spatial grid resolution, as $A \leqslant \frac{2}{\lambda}|\tilde{u}|^2$

3.4. **Constructing a latent image by image fusion.** With the video sequence $u(x, y, k)$ reconstructed from SOB+LAP, we combine these video frames to construct a sharp latent image. As in many related references, using mean or median is a reasonable choice to find an image with correct location information for each object. We also experimented with using the Sobolev approach on the temporal average, which seems to give a reasonably good latent image, as in Figure 4 (d). We further improve this latent image using an image fusion technique.

In order to improve the results from Figure 4 (d), we need to retain more details of the video frames. One of the most effective image restoration methods is the Non-local means (NLM) algorithm [3]. Its main idea is to replace the value of a certain pixel by the weighted average of the intensity values of its neighboring pixels for denoising purpose. The extension to video denoising is proposed in [4] where the neighborhood pixels are considered in three dimensions. This approach can be used as a fusion technique to further improve the latent image in Figure 4 (d). However, it has a limitation that, as in the case of using registration methods, it lacks a good template to compute the weight between itself and all the other images (the median image is blurry, while each video frame is sharp with oscillations).

We consider an approach similar to the so-called "Lucky Region" method [2] for image fusion. We first partition the image domain Ω into small sub-domains (image patches) Ω_j, such that

$$\Omega = \Omega_1 \bigcup \Omega_2 \bigcup \cdots \bigcup \Omega_M$$

and $\Omega_i \bigcap \Omega_j \neq \emptyset$ for any two adjacent neighboring image patches Ω_i and Ω_j. This is to ensure the compatibility between neighboring patches, that we assume two adjacent patches overlap with one column or one row as in Figure 6.

From these partitions, we select the best patch $u(\Omega_j, \hat{k})$ from all the frames for each Ω_j for $1 \leq k \leq N$. The best patch is selected by measuring two terms: the similarity to the mean and the sharpness. In particular, the similarity is measured using the L^2 distance to enforce the correct pixel location, while the sharpness is defined to be the variance of the patch. Note that there are other measurements of sharpness, such as H^1 semi-norm, kurtosis [7], entropy, etc. Here we use variance for simplicity.

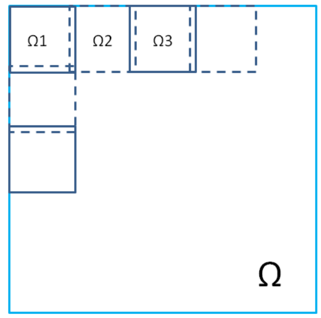

FIGURE 6. Partition of the image domain Ω. There is one row or one column overlap between two adjacent sub-regions Ω_i and Ω_j.

Suppose the video sequence $u(x, y, k)$ has a temporal mean $v(x, y)$, $v(x, y) = \frac{1}{N}\sum_k u(x, y, k)$. We find the index of the best frame by the following measure: For each patch Ω_j, find

$$\hat{k} = \max_{1\le k\le N} \left\{(1-\beta)\|u(x, y, k) - a(x, y)\|^2 + \beta\,\|u(x, y, k) - \bar{u}(k)\|^2\right\}.$$

Here $\bar{u}(k) = \frac{1}{|\Omega_j|}\int_{\Omega_j} u(x, y, k)\mathrm{d}x\mathrm{d}y$ is the patch mean on Ω_j, and the L^2 norm and the variance are computed on Ω_j as well. Here β is a parameter to balance two terms. We replace the patch values in the sub-domain Ω_j by $u(x, y, \hat{k})$. As for the overlapping region, we take the value which is an average among the patches that cover it.

Figure 7 shows the effect of this approach. Image (a) is Figure 5(d), which is the Sobolev sharpening on the temporal average (average first then deblur). Image (b) is the mean of the processed video SOB+LAP (deblur first then average), and Image (c) is the improvement by the lucky frame image fusion. Comparing (a) and (b) shows that it can give better results when each video frame is deblurred then followed by a diffeomorphism (averaging is considered here), which is consistent with [14]. The proposed method SOB+LAP not only sharpens each individual frame, but also normalizes the temporal direction at the same time. Therefore, image (b) is more regularized than just considering the diffeomorphism of sharp images. Using our lucky region technique, image (c) is even clearer. By using SOB+LAP, the straight edges of the rectangles, and especially around the small details, are well-recovered. The sharpness is by far the best, clearly showing the number 3 (on the bottom right corner of the image).

4. Numerical Experiments.

4.1. Video Reconstruction/Stabilization:

Figure 8, 9 and 10 illustrate the results of SOB+LAP. It is best seen in the videos posted at our project's website.[1] We plot a few frames from the video sequences. As shown in the beginning of this paper, two video sequences capture the same scene but at different times. For the mild turbulent motion in the morning, we can restore the sharp and straight bars using SOB+LAP, as shown in Figure 8. From the top row, (a)-(b) show the raw data, the second row (c)-(d) the reconstructions of using only SOB on each frames,

[1] https://sites.google.com/site/louyifei/research/turbulence

(a) (b) (c)

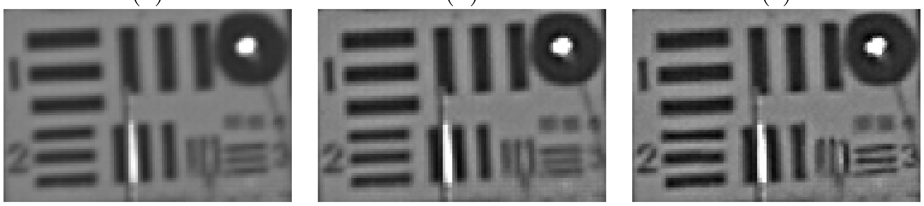

FIGURE 7. Latent Images: (a) This is Figure 5 (d)- applying SOB on the temporal mean. (b) The temporal mean of the video sequence after SOB+LAP. (c) Further improvement using our image fusion technique from the video reconstruction by SOB+LAP. In (c), notice the straight edges of the rectangles, and details are well-recovered, which clearly shows the number 3 (on the bottom right corner of the image).

and the third row (e)-(f), the reconstruction of SOB+LAP. Notice the second row may look sharper, yet the oscillations on the boundaries persist - they are more noticeable on the video. The proposed method SOB+LAP stabilizes the oscillation on the boundaries while recovering the sharpness, as shown in (e)-(f), compared to (b) the raw data and (d) SOB only on each frames.

Interlaced Video: A video sequence with interlacing is explored in Figure 9. The top row shows the original video sequence with interlacing. The video frames are preprocessed by taking the odd rows and interpolating the even rows. This new sequence is shown on the second row, Figure 9 (b). It shows less interlacing phenomena than the original sequence. The SOB result shown in the third row (c) and the SOB+LAP result shown in the fourth row (d) are applied to the preprocessed sequence in (b). Applying SOB for each frames makes the images sharper, yet the interlacing effect is emphasized. The sequence in (d), SOB+LAP is more stable and the interlacing effects are reduced. With the help of temporal diffusion, the small details - white squares around the black borders - are more coherent and clearer in sequence (d).

Moving object: Figure 10 illustrates a semi-synthetic example of a moving object in the video sequence. We artificially crop the region of interest so that the car moves forward for the first 15 frames, then forward and downwards for another 15 frames, that there is a discontinuity in the velocity of the car at the 15th frame. The first row shows the raw frames, the second row shows SOB and the third row shows SOB+LAP. Although the second row images appear sharp as individual image, the oscillations of the raw frames are not stabilized as a video sequence, and atmospheric turbulence effects are not corrected. SOB+LAP stabilizes the oscillations and the reconstructed video sequence shows smooth movement of the car. However, due to using the Laplacian operator in time, some ghost effects are present in the 15th frame where there is a shift in the movement of the car. Visually, the two bars in front of the car are doubled in the middle image of the row (c).

4.2. **Latent image reconstruction and comparisons.** Figures 11 and 12 are our proposed method and further improvements using image fusion techniques. These results are compared with [2], where the lucky-region fusion approach is used for atmospherically distorted images, and [17], an extension from [14] to a

(a) (b) zoom

(c) (d)

(e) (f)

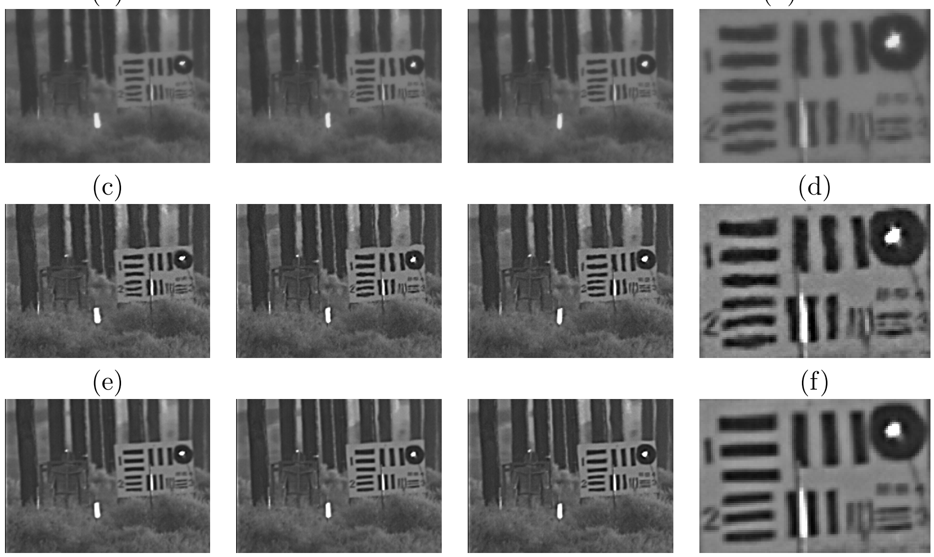

FIGURE 8. Reconstruction of the video sequence captured in the morning: The top row (a)-(b) is the raw data. The second row (c)-(d) is the reconstructions of SOB only. The third row (e)-(f) is reconstruction with SOB+LAP. The first three columns are the 10th, 20th and 30th frame from each video sequence. The last column (b), (d) and (f) shows the magnification of the target board in the 30th frame, i.e. the third column. SOB+LAP stabilizes the oscillation on the boundaries while recovering the sharpness.

variational model using Bregman iteration and operator splitting with optical flow. These two methods do not deal with the inherent blur in the original video sequence, so their outputs appear to be blurry. Image (d) is very sharp yet the oscillations of the rectangles are not completely corrected. Image (e) has a better recovery of the rectangles, yet using our image fusion technique can further improve the result as in (f).

4.3. **Challenging case - Afternoon turbulence.** Figure 13 presents the challenging case of atmospheric turbulence. The top row clearly illustrates the severity of the phenomenon. With SOB in the second row, the result looks sharper, yet the effects of such severe turbulence are still visible. The last row shows our result: even for this challenging example, the three bars on the top left corner of the pattern board are somewhat recovered and the video sequence is stabilized.

We analyze this difficulty by looking into the turbulence motion of the morning, Figure 8, and the afternoon, Figure 13. We first obtain a profile by tracking the edge of the rectangle along a particular line, as shown in Figure 14 (this example is of Figure 8). To automatically track their movement in the video sequence, we first apply the Canny edge detector to get a binary edge map, then we record the position of the edge points along the line. The plot, Figure 14 (b), shows only one-dimensional vertical changes, while the true motion is two-dimensional in space (and, the accuracy of the motion is in pixels). This is a rough estimate of the true

(a)

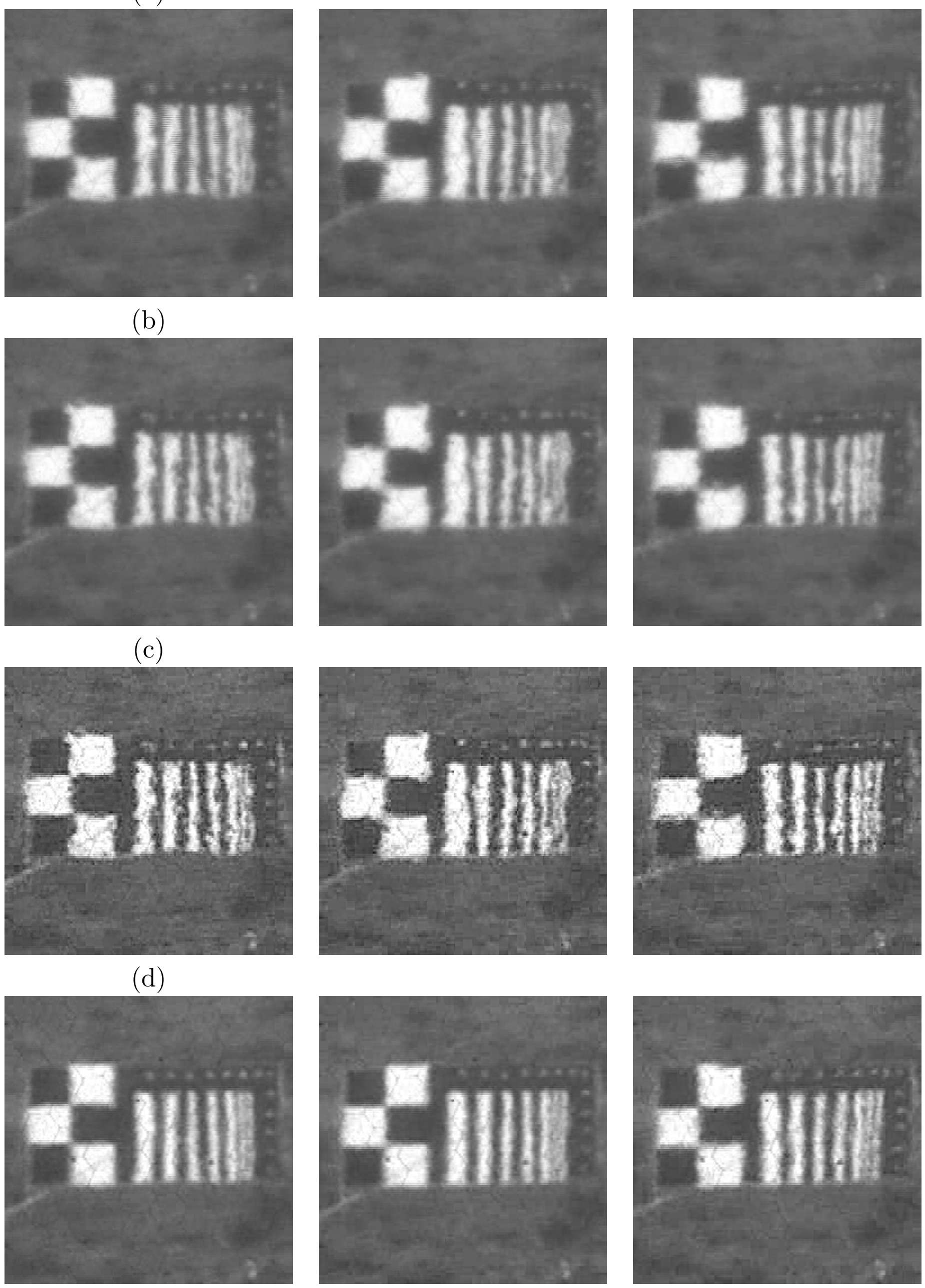

FIGURE 9. Reconstruction of a video sequence with interlacing: The top row (a) showing the original video with interlacing phenomenon. The second row (b) is the preprocessed raw data - still the interlacing effect is present. The third row (c) is the reconstruction of SOB only. The fourth row (c) is the reconstruction using SOB+LAP. In row (c), the interlacing effect is emphasized. The sequence in (d), SOB+LAP is more stable and interlacing effects are reduced. With the help of the temporal diffusion, the small details (white squares) around the black borders are more coherent and clearer in the row (d).

FIGURE 10. Reconstruction of a video sequence with a moving object. From top to bottom: the raw data, the reconstructions of SOB only and SOB+LAP. From left to right: the 5th, 15th and 25th frame. In the middle image of the row (c), the two bars in front of the car are doubled, due to the discontinuity of the car velocity and the time Laplacian in SOB+LAP.

motion, however, it shows that the motion is not individually random motion, but moves in a group which is consistent with using the wave models in literature.

We apply this tracking algorithm on a single point on two video sequences for Figure 8, and the afternoon, Figure 13. In Figure 15, two key points are marked as the blue dots in (a) and (b): the horizontal motion is tracked for (a) (the morning) and the vertical motion is tracked for (b) (the afternoon). The second row is the histogram of their positions through time. It is consistent with the finding in [23] that turbulent motion follows a Gaussian distribution. The third row shows the profile comparison of the blue dot movement of the original one and the SOB and SOB+LAP. Comparing the blue line (tracking of the key points) of (e) and (f), it is clear the afternoon turbulence is very severe compared to the morning case, due to the higher temperature during the day. Comparing the graphs, blue, red and green in image (e) and (f), it is clear that applying SOB on the each frames does not correct the temporal oscillation. However, SOB+LAP handles the oscillations well and stabilizes the motion, even in the case of severe oscillation in (f), notice the green line (SOB+LAP) is the most stable among the graphs.

5. **Concluding remarks.** We propose a simple and stable method to stabilize the video and to find a sharp latent image. Two of the main effects of atmospheric turbulence are temporal oscillation and blurry image frames, and we propose the method (14) that stabilizes the temporal oscillation and sharpening the video frame at the same time. The Sobolev gradient approach gives a natural deblurring in an anisotropic manner, while the temporal dimension is regularized with the Laplace

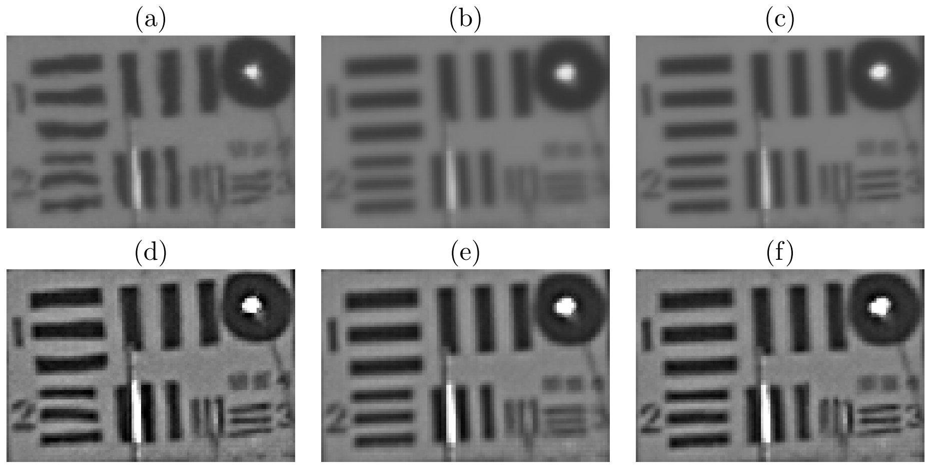

FIGURE 11. Latent image comparison: (a) One frame from the original sequence. (b) Using the lucky-region fusion [2]. (c) Using [17]. (d) One frame from SOB+LAP. (e) The temporal mean of SOB+LAP. (f) The proposed method to find the latent image, which is an improvement using image fusion technique from (d) or (f). Since the methods [2] and [17] do not deal with the inherent blur in the original video sequence, image (b) and (c) appear to be blurry. Image (d) is very sharp yet the oscillations of the rectangles are not completely corrected. Image (e) has a better recovery of the rectangles, yet using our image fusion technique can further improve the result as in (f).

operator. In addition, numerical computation is done using FFT, which makes the algorithm very fast and efficient. SOB+LAP is a simple and stable methods for video sequence stabilization and reconstruction. One of the challenges is to construct a good latent image, and from the video result of SOB+LAP, we computed the temporal average to get dependable latent images as in Figure 7 (a) and (b). We further improve the results using the lucky-region image fusion and construct an image such as Figure 7 (c). In some cases, the effects of atmospheric turbulence are so severe that no existing method can correct them, as shown in Section 4.3. Our algorithm performs in a way that is comparable with the state of the art, but still is unable to resolve fine details in the case of destructive turbulent degradation. This remains, therefore, an open problem with plenty of room for further investigation.

Acknowledgments. This paper is dedicated to Tony Chan on the occurence of his 60th birthday.

This work was supported by ONR grant N000141210040, NSF grants DMS-1118971 and DMS-0914856. The authors want to thank Dr. Jerome Gilles in UCLA and the members of the NATO SET156 (ex-SET072) Task Group for the opportunity of using the data collected by the group during the 2005 New Mexico field trials, and the Night Vision and Electronic Sensors Directorate (NVESD) for the data provided during the 2010 summer workshop. The authors would like to thank Dr. Alan Van Nevel at the U.S. Naval Air Warfare Center, Weapons Division

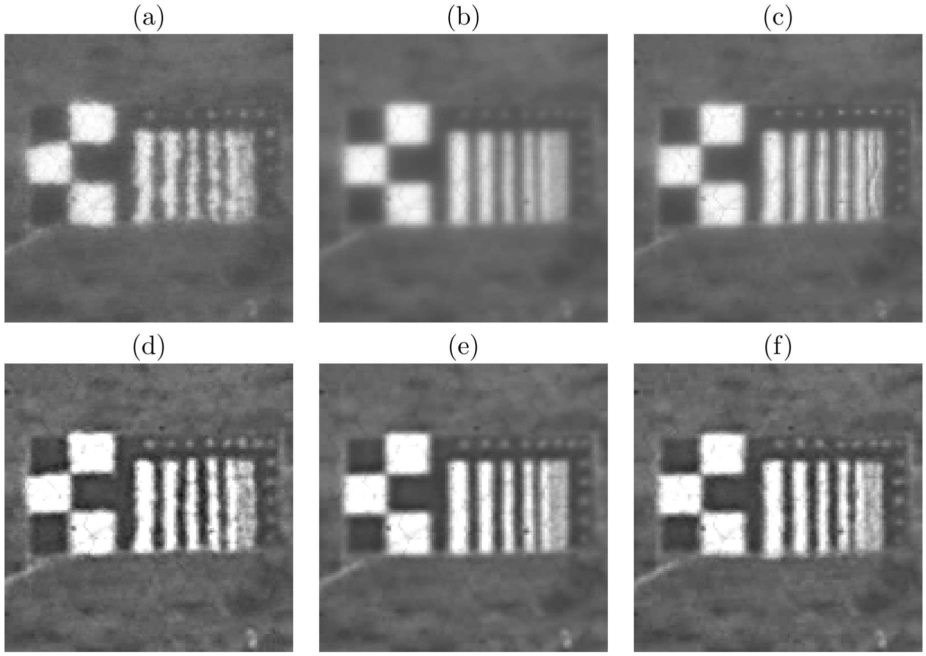

FIGURE 12. Latent image comparison: (a) One frame from the original sequence. (b) The lucky-region fusion [2]. (c) Using [17]. (d) One frame from SOB+LAP. (e) The temporal mean of SOB+LAP. (f) The proposed image fusion technique.

(China Lake, California) for providing some of the image data. The authors also thank Prof. Stanley Osher in UCLA and Dr. Yu Mao in University of Minnesota for helpful discussions.

REFERENCES

[1] L. Alvarez and L. Mazorra. Signal and image restoration using shock filters and anisotropic diffusion. *SIAM J. Numer. Anal.*, 31(2):590–065, 1994.

[2] M. Aubailly, M.A. Vorontsov, G. W. Carhat, and M. T. Valley. Automated video enhancement from a stream of atmospherically-distorted images: the lucky-region fusion approach. In *Proceedings of SPIE*, volume 7463, 2009.

[3] A. Buades, B. Coll, and J. M. Morel. A review of image denoising algorithms, with a new one. *Multiscale Modeling and Simulation*, 4(2):490–530, 2005.

[4] A. Buades, B. Coll, and J.M. Morel. Nonlocal image and movie denoising. *International Journal of Computer Vision*, 76(2):123–139, 2008.

[5] K. Buskila, S. Towito, E. Shmuel, R. Levi, N. Kopeika, K. Krapels, R. Driggers, R. Vollmerhausen, and C. Halford. Atmospheric modulation transfer function in the infrared. *Appl. Opt.*, 43:471–482, 2004.

[6] J. Calder, A. Mansouri, and A. Yezzi. image sharpening via Sobolev gradient flows. *SIAM J. Imaging Sciences*, 3(4):981–1014, 2010.

[7] J. Caviedes and S. Gurbuz. No-reference sharpness metric based on local edge kurtosis. In *IEEE International Conference on Image Processing*, volume 3, pages 53–56, 2002.

[8] D. Frakes, J. Monaco, and M. Smith. Suppression of atmospheric turbulence in video using an adaptive control grid interpolation approach. In *IEEE International Conference on Acoustics, Speech and Signal processing (ICASSP)*, volume 3, pages 1881–1884, 2001.

FIGURE 13. Reconstruction of a video sequence captured in the afternoon: The top row (a)-(b) is the raw data. The second row (c)-(d) is the reconstructions of SOB only. The third row (e)-(f) is reconstruction with SOB+LAP. The first three columns are the 10th, 20th and 30th frame from each video sequence. The last column (b), (d) and (f) shows the magnification of the target board in the 30th frame, i.e. the third column. SOB+LAP stabilizes the oscillations on the boundaries while recovering the sharpness.

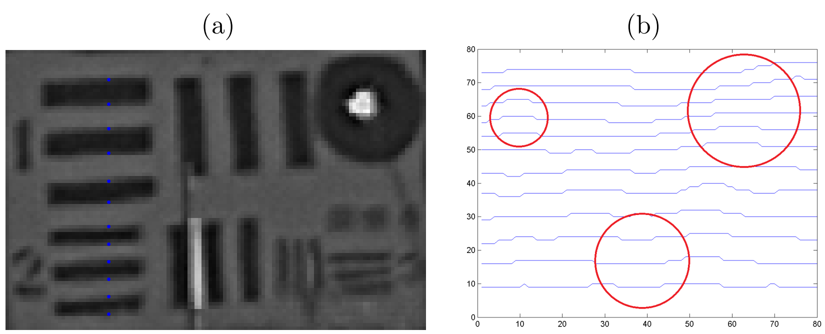

FIGURE 14. The positioning of the key points along a line. The key points are displayed as the blue dots on (a). (b) shows how these points are oscillating can time t changes. As indicated with the red circles, this graph demonstrates that the wave movement of the turbulence happens in groups.

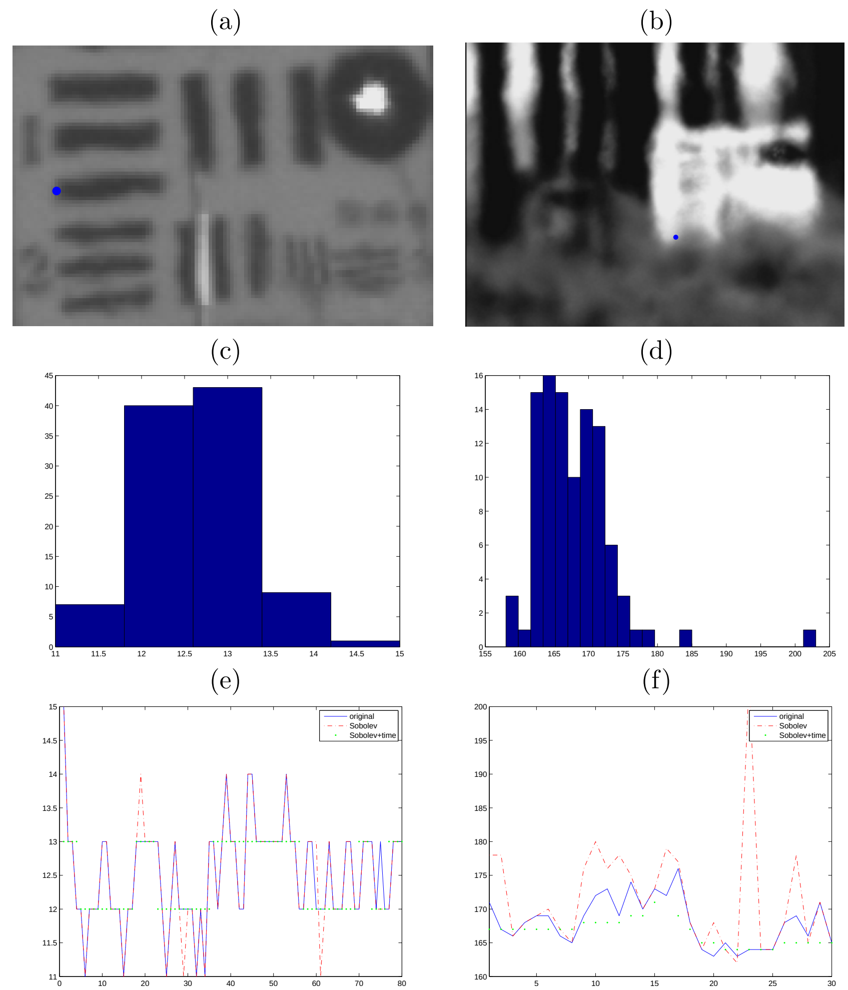

FIGURE 15. The tracking profile of one particular point on two videos marked in blue in (a) and (b), with its horizontal motion in the morning and vertical motion in the afternoon respectively. In (c) and (d), the histogram of their positioning profile demonstrates that the turbulent motion follows a Gaussian distribution. In (e) and (f), we compare the profiles of the original sequence and the reconstructions of SOB and SOB+LAP. The green lines (SOB+LAP) are the most stable among the graphs, showing the effect of the time Laplacian.

[9] D. L. Fried. Optical resolution through a randomly inhomogeneous medium for very long and very short exposures. *J. Opt. Soc. Am.*, 56:13721379, 1966.

[10] S. Gepshtein, A. Shtainman, B. Fishbain, and L.P. Yaroslavsky. Restoration of atmospheric turbulent video containing real motion using rank filtering and elastic image registration. In *Proceeding of the Eusipco*, 2004.

[11] J. Gilles and S. Osher. Fried deconvolution. *UCLA CAM report 11-62*, 2011.

[12] M. Hirsch, S. Sra, B. Scholkopf, and S. Harmeling. Efficient filter flow for space-variant multiframe blind deconvolution. *IEEE Conference on CVPR*, pages 607 – 614, 2010.

[13] R. E. Hufnagel and N. R. Stanley. Modulation transfer function associated with image transmission through turbulence media. *J. Opt. Soc. Amer. A, Opt. Image Sci.*, 54(1):52–61, 1964.
[14] J.Gilles, T. Dagobert, and C. De Franchis. Atmospheric turbulence restoration by diffeomorphism image registration and blind deconvolution. In *Advanced Concepts for Intelligent Vision Systems (ACIVS)*, Oct 2008.
[15] D. Li, R. Mersereau, and S. Simske. Atmospheric turbulence degraded image restoration using principal components analysis. *IEEE Geoscience and Remote Sensing Letters*, 4(3), 2007.
[16] D. Li and S. Simske. Atmospheric turbulence degraded-image restoration by kurtosis minimization. *IEEE Geoscience and Remote Sensing Letters*, 6(2), 2009.
[17] Y. Mao and J. Gilles. Non rigid geometric distortions correction - application to atmospheric turbulence stabilization. *Inverse Problems and Imaging, to appear*, 2012.
[18] Stefano Soatto Mario Micheli, Yifei Lou and Andrea L. Bertozzi. A dynamic texture model for imaging through turbulence. *UCLA CAM report 12-01*, January 2012.
[19] A. Marquina. Nonlinear inverse scale space methods for total variation blind deconvolution. *SIAM J. of Imaging Sciences*, 2(1), 2009.
[20] P. Perona and J. Malik. Scale-space and edge detection using anisotropic diffusion. *IEEE Trans. Pattern Anal. Mach. Intell.*, 12:629–639, 1990.
[21] J. Ricklin and F. Davidson. Atmospheric turbulence effects on a partially coherent gaussian beam: implications for free-space laser communication. *J. Opt. Soc. Am. A*, pages 1794–1802, 2002.
[22] M. Roggemann and B. Welsh. *Imaging Through Turbulence*. CRC Press, Boca Raton, FL, 1996.
[23] M. Shimizu, S. Yoshimura, M. Tanaka, and M. Okutomi. Super-resolution from image sequence under influence of hot-air optical turbulence. In *IEEE Computer Vision and Pattern Recognition (CVPR)*, pages 1–8, 2008.
[24] D. Tofsted. Reanalysis of turbulence effects on short-exposure passive imaging. *Optical Engineering*, 50(1):016001, 2011.
[25] M. A. Vorontsov and G. W. Carhart. Anisoplanatic imaging through turbulent media: image recovery by local information fusion from a set of short-exposure images. *J. Opt. Soc. Am. A*, 18:1312–1324, 2001.
[26] P. Zhang, W. Gong, X. Shen, and S. Han. Correlated imaging through atmospheric turbulence. *Phys. Rev. A*, 82:033817, 2010.
[27] X. Zhu and P. Milanfar. Image reconstruction from videos distorted by atmospheric turbulence. In *SPIE Electronic Imaging, Conference on Visual Information Processing and Communication*, 2010.
[28] X. Zhu and P. Milanfar. Removing atmospheric turbulence. *Submitted to IEEE Trans. on Pattern Analysis and Machine Intelligence*, 2011.
[29] X. Zhu and P. Milanfar. Stabilizing and deblurring atmospheric turbulence. In *International Conference on Computational Photography (ICCP)*, 2011.

Received xxxx 20xx; revised xxxx 20xx.

E-mail address: louyifei@gmail.com
E-mail address: kang@math.gatech.edu
E-mail address: soatto@cs.ucla.edu
E-mail address: bertozzi@math.ucla.edu